Magnetic Flux Cancelation as the Buildup and Trigger Mechanism for CME-Producing Eruptions in two Small Active Regions

Alphonse C. Sterling[1], Ronald L. Moore[1,2], Navdeep K. Panesar[1]

Received _____; accepted _____

Accepted for publication in The Astrophysical Journal

[1]NASA Marshall Space Flight Center, Huntsville, AL 35812, USA,
alphonse.sterling@nasa.gov, ron.moore@nasa.gov

[2]Center for Space Plasma and Aeronomic Research, University of Alabama in Huntsville, AL 35899, USA

ABSTRACT

We follow two small, magnetically isolated CME-producing solar active regions (ARs) from the time of their emergence until the time that their core regions erupt to produce the CMEs several days later. In both cases, magnetograms show: (a) following an initial period where the poles of the emerging regions separate from each other, the poles then reverse direction and start to retract inward; (b) during the retraction period, flux cancelation occurs along the main neutral line of the regions, (c) this cancelation builds the sheared core field/flux rope that eventually erupts to make the CME. In the two cases, respectively 30% and 50% of the maximum flux of the region cancels prior to the eruption. Recent studies indicate that solar coronal jets frequently result from small-scale filaments eruptions, with those "minifilament" eruptions also being built up and triggered by cancelation of magnetic flux. Together, the small-AR eruptions here and the coronal jet results suggest that isolated bipolar regions tend to erupt before or when a threshold of roughly 50% of the region's maximum flux has canceled. Our observed erupting filaments/flux ropes form at sites of flux cancelation, in agreement with previous observations. Thus, the recent finding that minifilaments that erupt to form jets also form via flux cancelation is further evidence that minifilaments are small-scale versions of the long-studied full-sized filaments.

Subject headings: Sun: activity — Sun: filaments — Sun: flares — Sun: magnetic fields — Sun: UV radiation

1. Introduction

Large-scale solar eruptions that produce solar flares, coronal mass ejections (CMEs), and other phenomena often start with the eruption of a filament structure of size 3×10^4—1.1×10^5 km Bernasconi et al. (2005). What builds these filaments, and what eventually triggers them to undergo violent eruption, are long-standing questions. Because filaments form in magnetic field that runs along a magnetic neutral line, it is clear that magnetic free energy, i.e. energy in the field in excess of that of a potential configuration, is a requirement. Magnetic flux cancelation at the neutral line has been observed to precede filament formation (Martin 1986), and van Ballegooijen & Martens (1989) developed a theoretical picture explaining how such cancelation can result in a filament.

Among the questions that remain is: what are the specific circumstances that determine when the filament will erupt to produce a flare and, if ejective, a CME? It is a challenge to address this question with large-scale eruptions for the following reason: CME-producing filament eruptions often occur in active regions (ARs) that emerge and grow to a substantial size before eruption takes place; apparently, frequently the field must first evolve over some time after the region emerges, and so it can take two weeks or more for the AR to mature and generate a strong solar eruption. Therefore, because a complete solar rotation is $\sim$27 days, it is often not possible to observe the same flare-producing AR on the Sun from the time that AR is born until the time of eruption. That is, the AR in which a large-scale eruption visible from Earth occurs usually was born when that region was on the far side of the Sun, if not even earlier. This means that it is frequently not possible to follow in its entirety the magnetic buildup of a large-scale solar eruption with a set of near-Earth instruments. This makes it difficult to observe the entire history leading up to the eruption, and so our understanding of the eruption's buildup is frequently limited in scope. And, because the time-scale for buildup to eruption is comparatively long, it can be difficult to

separate out the key aspects that are most important for understanding eruption onset. That is, if a strong-flare-producing AR develops on the far side of the Sun, we could miss key magnetic changes leading to an eruption in the AR when it is on the near side. Sorting out which magnetic changes are key to an eruption are made more difficult in such cases.

It therefore would be advantageous if there were short-lived small magnetic active regions that we could study in their entirety during their disk passage, and over a short-enough period so that the chance of complicating other substantial magnetic flux changes occurring during the build-up to a whole-region-scale eruption would be minimized. One such category of such small active solar magnetic regions are those whose whole-region-scale eruptions make *solar coronal jets*. Sterling et al. (2015) present evidence that these jets are small-scale versions of larger-scale eruptions (see, e.g., Innes & Teriaca 2013, for a similar view), implying that lessons from jet-producing regions can inform us about larger-scale-eruption regions.

Seen in X-rays with *Hinode*/XRT, coronal jets are long (reaching ∼50,000 km), narrow (∼8,000 km), transient (lifetime ∼10 min) features that shoot into the corona at a rate of ∼60/day in polar coronal holes (Cirtain et al. 2007; Savcheva et al. 2007), and a "jet bright point" (JBP) forms at an edge of the base of the jet. Coronal jets are also visible in EUV coronal images (e.g. Raouafi et al. 2008; Nisticò 2009), and they are prevalent in quiet Sun and ARs in addition to coronal holes (e.g. Shimojo et al. 1996; Raouafi et al. 2016; Panesar et al. 2017, 2018; Sterling et al. 2017; Hong et al. 2016, 2017). Figure 1 shows a schematic picture for jet production presented by Sterling et al. (2015), based on the idea that eruption of a small-scale filament, or "minifilament," is the source of the jets. This figure is modified slightly from earlier versions (Sterling et al. 2015, 2016, 2017) with the addition of the red, dashed reconnected field lines in panel (b), motivated by a recent study of Moore, Sterling, & Panesar (2018) demonstrating that reconnection at the magnetic

null point in the corona often begins earlier than or concurrent with the tether-cutting reconnection below the rising minifilament.

Based on recent observations, it is now clear that at least many coronal jets are small-scale versions of large-scale eruptions (e.g. Shen et al. 2012; Adams et al. 2014; Sterling et al. 2015, 2016, 2017; Panesar et al. 2016a,b, 2017, 2018). Seen in profile at the solar limb, the minifilaments that erupt to cause the jets are of a much smaller size ($\sim$8000 km) but otherwise appear to be similar to "normal"-sized filaments.

There are direct analogies between the coronal jets, and the the large-scale magnetic eruptions that make flares and CMEs: coronal jets result from eruptions of minifilaments, generate a miniature flare (the JBP), and eject material onto open field lines that guide the jet (analogous to the CME in many large-scale eruptions) (Sterling et al. 2015). Besides physical size, another difference between larger-scale eruptions and the eruptions that make jets is that the buildup to eruption is much shorter with the jets: Panesar et al. (2017) found that, for ten solar quiet region jets, the minifilaments that erupt to make jets evolve from birth to eruption over periods ranging from 1.5 hr to two days, and thus much shorter than the two weeks or more for the ARs hosting large-scale eruptions to evolve and release an explosive eruption.

Because the erupting minifilaments are analogous to the erupting larger-scale filaments, we suspect that the mechanism building and triggering the minifilaments to erupt is the same, expect for size scale (and magnitude), as the buildup and triggering mechanism for large-scale eruptions. Minifilaments that erupt to form jets evolve rapidly enough so that we can investigate directly the magnetic flux changes leading to their eruption. Over several investigations (§2) we have now measured magnetic-change quantities of the fields at the base of a number of jets. The object of the current study is to examine the magnetic properties of a CME-producing region that is larger scale than than those that produce jets,

for comparison with the situation in jets. Our selected erupting region however is small enough so that we can observe the region from the time of that field's emergence through the time of eruption. This allows us to measure in this CME-producing eruption the same magnetic quantities that we measured in the jets.

2. Magnetic Cancelation in Jets

We have previously studied the properties of the flux cancelations around the time of jet onset. Panesar et al. (2016b, 2017) examined 10-15 quiet-region jets (the actual number studied depends on how one counts repeated, a.k.a. homologous, jets); and Panesar et al. (2018) studied 13 coronal hole jets. All of the quiet region and coronal hole jets either showed clear flux cancelation at about the time of the jet onset, or (in a minority of cases) the situation was ambiguous but still consistent with cancelation. In the AR-jet cases (Sterling et al. 2016, 2017), in only one (out of ≈17 in total) jet episode (in Sterling et al. 2016) was it unclear whether cancelation was occurring at the jet location near the time of jet onset; in all other cases, cancelation was clearly present at the base of the jets at the time the jets were occurring.

For the nine quiet region jets where reliable measurements were possible, Panesar et al. (2016b) found that, between a time substantially before the jet (5—6 hrs) and soon after the jet (0—1 hrs), the percentage of minority-flux reduction ranged between 18%—57%. From the reduction percentage for each jet (which we call p_i) and their corresponding standard deviations (σ_i), using the listed in Table 1 of Panesar et al. (2016b) we can calculate a weighted mean, $\overline{P}$, and weighted standard deviation, $\sigma_{\overline{P}}$, for the percent reduction in flux for each of those quiet region jets. Using $1/\sigma_i^2$ as weighting factors, we use for these quantities (e.g., Bevington & Robinson 2003):

$$\overline{P} = \frac{\sum_{i=1}^{N} p_i/\sigma_i^2}{\sum_{n=1}^{N} 1/\sigma_i^2}, \tag{1}$$

and

$$\sigma_{\overline{P}}^2 = \frac{N \sum_{n=1}^{N} (p_i - \overline{P})^2/\sigma_i^2}{(N-1) \sum_{n=1}^{N} 1/\sigma_i^2}, \tag{2}$$

where N is the number of jets examined. This gives a weighted mean and weighted standard deviation of 36.6%±12.8% for the nine quiet Sun jets. Also, for these quiet Sun jets Panesar et al. (2016b) found the minority flux patches generally to be of order $\sim 10^{19}$ Mx.

In a similar fashion, for coronal hole jets Panesar et al. (2018) found flux reductions for 11 jets to range between 21%—73%. Applying (1) and (2) to the values in Table 1 of Panesar et al. (2018) gives weighted average and weighted standard deviation of 44.8%±15.8%. For these coronal hole jets, Panesar et al. (2018) found the minority flux patches again generally to be of order $\sim 10^{19}$ Mx, and they also calculated an average cancelation rate of $\sim 0.6 \times 10^{18}$ Mx/hr.

For approximately seven AR jets, Sterling et al. (2017) found on average $\sim 5 \times 10^{18}$ Mx canceled prior to each jet episode, that the flux cancelation occurred at a rate of $\sim 1.5 \times 10^{19}$ Mx/hr, and estimated that $\sim 10^{28}$—$\sim 10^{29}$ ergs of free magnetic energy built up per jet. Due to the dynamic nature and polarity-arrangement complexity of the region however, it was not as straightforward as in the quiet Sun and coronal hole cases to measure the percentage of flux change in the buildups to the jets in the Sterling et al. (2017) study. We summarize various coronal jet properties in Table 1.

Several other detailed investigations of one or a small number of jets also found them

to originate from locations where magnetic flux cancelation occurs (Hong et al. 2011; Huang et al. 2012; Adams et al. 2014; Young & Muglach 2014a,b). Some other jets however apparently occur in the absence of obvious flux cancelation at the HMI-detectable level (Kumar et al. 2018), although a study of 20 jets by Mulay et al. (2016) also supports that most jets do occur at sites that include obvious flux cancelation.

Here we will study two CME-producing ARs for which we can track the entire magnetic history of the regions, from time of emergence until the time of the CME-producing eruptions.

3. Instrumentation and Data

For this study we use data from two instruments on the Solar Dynamics Observatory (SDO). That satellite's Atmospheric Imaging Assembly (AIA; Lemen et al. 2012) images the Sun in seven EUV wavelength bands: 304 Å, 171 Å, 193 Å, 211 Å, 131 Å, 94 Å, 335 Å, in two UV bands: 1600 Å and 1700 Å, and in a visible band: 4500 Å. These channels respond to plasmas emitting over a wide range of temperatures in the solar atmosphere (Lemen et al. 2012), observing the full disk with $0''.6$ pixels and typically with cadence of 12 s and 24 s in the EUV and UV channels respectively. Our magnetic data are from full-disk line-of-sight magnetograms from *SDO*'s Helioseismic and Magnetic Imager (HMI; Scherrer et al. 2012), with 45 s cadence and $0''.5$ pixels.

For this study we searched for ARs that (a) erupt to produce a CME, (b) that we can follow on the solar disk from emergence until the time of eruption within a single disk passage, and (c) that remain well isolated from other magnetic flux emergence until the time of eruption. Additionally, because we want to track the region as it builds up the free energy in the field that eventually erupts, we avoided regions that emerge already

containing substantial free energy concentrated in their cores and can explosively erupt shortly after emergence, such as is the case with some delta-sunspot ARs.

For our two selected regions, because of the short development time necessitated by condition (b), in both cases the emerged AR is small and the resulting CME-producing eruptions are correspondingly small. Our first example makes a CME-producing eruption with a *GOES* C-class flare of 2013 October 20 from AR 11868. This region had small sunspots visible on October 18. Also, it had two filament/flux ropes, one along the region's main neutral line that was faint in EUV, and a second one along a neutral line on the outside edge of the region; as we will discuss below, both filaments erupted in this region's eruption episode. The second active region that we study produced a B-class flare on 2010 July 16 from AR 11088; this region had a small sunspot from early in its life that decayed over the course of our observations. This second region also had a filament prominent in EUV running along its main neutral line, and this filament erupted during the eruption episode.

In both cases the resulting CMEs had widths smaller than many larger eruptions (as discussed below). On the other hand, in both cases the erupting filaments had 2-D projected spans (i.e., not considering inclination angle on the disk or curvature of the filament) of $\sim$70″; this is substantially longer than the $\sim$8000 km ($\sim$11″) for minifilaments measured in polar coronal hole jets by Sterling et al. (2015), or the jet-base widths for on-disk jets in coronal holes ($\sim$12,000 km)($\sim$17″) of Panesar et al. (2018) and in quiet regions ($\sim$17,000 km)($\sim$23″) of Panesar et al. (2016b). Therefore, we are observing eruptions of a larger category than those producing typical coronal jets.

4. Eruption of 2013 October 20

4.1. EUV Development

Figure 2 shows the eruption of 2013 October 20 in AIA 131 and AIA 304 Å images at various times, with Figures 2(d) and 2(h) showing overlaid HMI magnetograms. In describing this eruption, we will also point out similarities with coronal jets.

Figures 2(a)—2(c) show that one of the two flux rope/filaments of this region erupts out from the main neutral line (Fig. 2(d)), where that neutral line is apparent in the magnetograms of Figures 2(d) and 2(h). This flux rope/filament is not very prominent in EUV; while visible in all seven AIA EUV channels, it is perhaps most obvious in the close-up 304 Å images of Figures 2(a)—2(c). (At times leading up to eruption, this filament is prominent in GONG Hα images, available at gong.nso.edu. Discussion of these images however is outside the focus of the current paper.) The main flare brightening of the eruption occurs on the same main, strong magnetic neutral line (Figs. 2(d) and 2(e)). Comparing with the jet picture, this main neutral line corresponds to the neutral line defined by polarities M2 and M2 in Figure 1(a), where the JBP develops in Figures 1(b) and 1(c)).

Away from that core location where the main brightening occurs, there is a bright rim that partially surrounds the core erupting region; arrows in Figure 2(e) point out these remote brightenings, which are also seen in some ejective flares (e.g. Masson et al. 2009; Sun et al. 2012; Joshi et al. 2015); Joshi et al. (2017) have argued that "three-ribbon flare" events such as this are closely analogous to jets. Circular ribbons such as these, sometimes seen as only a portion of circles, are common in coronal jets (e.g., li et al. 2017, 2018; Panesar et al. 2016b, Fig. 1b), and also in chromospheric jets known as surges (see discussion in Sterling et al. 2016, §4). Comparing these circular brightenings with

magnetograms (Fig. 2(h); also see Fig. 5(a)), it is obvious that they are lodged against the edge of dominant-polarity (negative in this case) field. This agrees with the jet picture in Figure 1, where the circular ribbon is mapped out by the negative-polarity footpoint of the dashed-line reconnection loop in Figure 1(b). For the eruption in Figure 2, the loops in the large-scale event corresponding to the Figure 1(b) dashed loop itself are visible in the AIA 131 Å video corresponding to Figure 2 (many such loops are obvious at, e.g., 09:23:44 UT in that video).

Our particular event in Figure 2 however is more complicated than the basic jet picture of Figure 1. In the core region, where the flare starts to brighten from about 08:32 UT in the video accompanying Figure 2, as noted above, in EUV images a well-developed filament does not form and the flux rope that erupts is faint (Figs. 2(a)—2(c)). There is, on the other hand, a large filament that forms at and erupts from a location in-between the core (where the bright flare is occurring in Fig. 2(b)) and the remote brightenings marked by the arrows in Figure 2(e). This filament begins to erupt at about 08:44 UT on 2013 October 20, which is after the core eruption starts at about 08:34 UT. We discuss this filament eruption further in §4.3.

Figure 3 and the accompanying video show that this region's eruption produced a CME, visible in *SOHO*/LASCO/C2 running-difference images (obtained from the online *SOHO*/LASCO CME catalog; Gopalswamy et al. 2009), first visible off of the solar west limb at 09:12 UT, and eventually having width $\sim 60^\circ$. It is likely that the CME has components from the eruption of the core-region flux rope, as well as from the eruption of the prominent filament, with both eruptions visible in the videos accompanying Figure 2.

4.2. Magnetic Field Evolution

From HMI magnetograms, AR 11868, from which the 2013 October 20 eruption occurred, started emerging at about 14:00 UT on 2013 October 15. It underwent a surge in emergence from about 04:00 UT on October 16, and an even stronger surge from about 02:30 UT on October 18. When it started emerging on October 15 it was about 400″ east of central meridian, and at the time of eruption near 08:40 UT on October 20 it is 500″ west of central meridian. Therefore it is an ideal example of a small bipolar AR with a relatively short evolution period of about five days, before producing an eruption. Moreover, the eruption was substantially larger (in both geometric size and EUV flux) than a coronal jet, and also drove a CME of modest width.

Figure 4 shows the evolution of the magnetic region, where we have rotated all of the images to a common time of 09:00 UT on 2013 October 20, and so close to the eruption time; all of the other presented solar images and movies for this event are rotated to this same time. In the images of Figure 4 we only show the region from after the start of the strongest surge in emergence, while the movie accompanying that figure shows the region's evolution over the entire time period, beginning before its emergence on October 14.

From Figure 4 and the accompanying movie, we see that the two polarities of the region first separate from each other, and that separating motion continues until around 03:00 UT on October 19. But then *the two polarities start to converge upon themselves.* As that convergence continues, the two poles of the bipole region start to interact and cancel, from about 03:00 UT on October 20, and this convergence and cancelation continues through the time of the eruption near 08:40 UT on October 20.

Figure 5 is a different representation of this dynamical evolution over the time span covered by Figure 4, that is, from the start of the final burst of flux emergence thorough to the time of the eruption. This is a time-distance map of that evolution, with the ordinate

values representing horizontal integrations across the region covered by the white box in Figure 4(a), plotted as a function of time; the vertical axis in Figure 5 therefore represents distance along the y-direction in the panels of Figure 4. This clearly shows the two flux polarities separating early during the period, and then converging at later times, with the eruption occurring near the time when strong patches of the opposite polarities collide.

Figure 6 shows the time evolution of the positive flux of the region, integrated over the area of the white box in Figure 4(a). Although the HMI magnetograms that we are using only provide the line-of-sight component, we have approximately accounted for foreshortening in the Earth-directed projection of that component by dividing by the cosine of the heliocentric angle between the AR's location and disk center (as observed by HMI), as a function of time. (When using non-derotated magnetograms, there is an additional cosine factor required to correct for foreshortening of the area used in the flux calculation, meaning that one should divide by cosine squared instead of cosine. Correction to this area factor however was accounted for with the derotation procedure that we used, which was the solarsoft (Freeland & Handy 1998) routine "drot_map," and therefore here we only need to divide by cosine to the first power.) We only measure the positive-polarity flux because it can be well isolated within the box over the entire duration of the measurement shown in Figure 6. In contrast, the negative flux has obvious flows across the Figure 4(a)-box boundary, and hence cannot be measured reliably over that region. Our plot in Figure 6 covers the entire period from the beginning of the flux emergence, showing the weak initial emergence near 14:00 UT on October 15, and then the two subsequent surges in emergence. This shows that when eruption occurs (orange line), the cancelation has been going on for some time.

Using the best-fit green line in the Figure 6 plot, we estimate the rate of flux cancelation to be 1.1×10^{19} Mx/hr over the full time period of the green line (30.75 hr; see Fig. 6

caption). If however we instead consider that the true fall-off commences with the bump in flux near 18:00 UT on October 19, then the rate increases to $\sim 1.5 \times 10^{19}$ Mx/hr. Therefore we take the rate of flux decrease to be $\sim (1.3 \pm 0.2) \times 10^{19}$ Mx/hr. If we assume that this canceled flux builds a magnetic flux rope, and assuming equal amounts of positive and negative flux cancel, this implies $\sim 3.9 \times 10^{20}$ Mx of flux builds up in the flux rope over a 30-hr period prior to the eruption. (The arguments are essentially unchanged if, instead of a flux rope, the cancelation goes into accumulation of non-potential shear along the neutral line.) From the plot in Figure 6 we see that $\sim$30% of the peak flux value canceled prior to the time of the eruption.

We can estimate the amount of free energy contained in, say, the flux rope, formed by the canceled field. We can estimate the magnetic field strength, B, of the flux rope, assuming that the total accumulated flux passes through the approximate length-wise cross-sectional area, A, of the flux rope. We estimate the size of the neutral line over which the cancelation occurs to be $\sim 50''$, based on the length of the abutting positive and negative fluxes in Figure 4(d)—4(f). Also, from Figure 4(f) we estimate, from the separation of the two abutting polarities, that the width of the flux rope might be roughly $5''$; this is about the separation distance between the positive and negative flux patches in Figures 4(e) and 4(f), the latter image being about three hours after the eruption occurred. We also assume the height of the cancelation region to be the same as the width, $5''$. So the total accumulated flux determined above would be $BA = 3.9 \times 10^{20}$, giving $B \sim 300$ G. With this value, and with the above dimensions for the flux rope, we can estimate the amount of energy built up in the flux rope volume, V ($= A \times$ (width of $5''$)). Considering the roughness in estimates for the flux rope size and in the magnetic field strength, we estimate the accumulated energy$= B^2/(8\pi)$ to be $\approx 2 \times 10^{30}$ erg. With a wider flux rope and/or larger magnetic field strength the estimate could be substantially higher, and so we can say the accumulated energy is $\sim 10^{30}$—10^{31} erg.

4.3. Filament Formation and Ejection

We next examine the development of the second filament (the one that was prominent in EUV images) that erupted with this event; in particular this question is of interest because, as discussed above, the filament did not form and erupt from the main neutral line of the AR. Looking at a 304 Å movie of the AR from near the time of its emergence until time of eruption (video accompanying Fig. 2) shows that the filament in the region develops over about 10—16 UT on October 18. From magnetograms overlaid onto those images (Figs. 2(e) and 2(h)) and the accompanying video (and also the magnetogram video accompanying Fig. 4), it is apparent that the filament forms where positive-polarity flux elements outside and to the west of the positive polarity pole of the emerging flux, canceled with surrounding negative-polarity field over about that same time period. From magnetogram images from about the time of Figure 4(b), we measure the filament-forming canceling elements to be of moderate strength, of ∼100—300 G; arrows in Figure 4(b) point to some of these flux elements. These values are substantially weaker than the strongest-field portions of the emerging region at that time, which have strengths ranging from ∼500 G and up to and exceeding 1000 G. Thus it is the intermediate-strength clumps that cancel to make the filament, rather than the strongest-field elements. These observations of flux cancelation as the mechanism for formation of the filament are fully consistent with previous observational and theoretical studies (e.g. Martin 1986; van Ballegooijen & Martens 1989). The canceling fluxes that form the filament are not concentrated enough to allow for easy isolation and flux-buildup and flux-rate measurements, as we did above with the canceling fluxes in the core region, and therefore we do not attempt such measurements here.

Eruption of the filament begins with its liftoff from the surface, which starts at about 08:41 UT on October 20; this is clearly later than the 08:32 UT start of the flare in the core region. Moreover, as the filament begins lifting off, remote ribbons of the region (arrows in

Fig. 2(e)) are also already illuminated. This means that new loops are being added to the lobe overlaying that filament, as at that point the eruption is in a situation analogous to Figure 1(b) in the jet picture (where the filament of this October 20 eruption initially sits beneath the central, larger lobe rooted in polarities M1 and M2 of Fig. 1(a)). We suspect that eruption of the filament is nonetheless triggered by the disruption resulting from the flux rope eruption along the main neutral line. Although it might seem counterintuitive to have the filament erupt through an overlying lobe that contains newly closed field (the dashed red loop in Fig. 1(b)), we have seen evidence before (Sterling et al. 2014) for where a strong second-stage filament erupted, apparently bursting through (or partially navigating around) newly closed field resulting from a first-stage eruption. Török et al. (2011) present another example of eruption through newly-closed field, along with numerical simulations demonstrating the plausibility of such complex eruptions. A likely possibility is that implosion of the field around the erupting core-region flux rope triggers the eruption of the remote filament, the so-called "Hudson Effect," from the ideas presented in Hudson (2000) (Janse & Low 2007; Panesar et al. 2013).

5. Eruption of 2010 July 16

Our second example is of AR 11088, which emerged on 2010 July 11 and resulted in a *GOES* B-class flare five days later on July 16. Figure 7 shows AIA 171 Å and 304 Å images of this event. In this case a filament erupted from the main neutral line of the region, and was directed toward Earth, and hence toward AIA. From the accompanying video, the eruption begins near 15:00 UT, with strong flare emission apparent about 20 min later.

Figure 8 and the accompanying video show that a CME that likely originated from this eruption was visible in *STEREO*-B COR 1 images (from the online COR1 CME catalog: cor1.gsfc.nasa.gov/catalog/), beginning from 15:41:02 UT on 2010 July 16, and,

from Figure 8(b), obtaining a width of approximately 35°. Similarly *STEREO*-A COR 1 shows what is likely the same CME from 16:30:18 UT. *SOHO*/LASCO does not show a clear CME from this region, likely due to the CME's small width and on-disk location not far from disk center from the LASCO perspective.

Figure 9 shows the magnetic evolution of AR 11088, the source of this eruption, over the five-day period from the region's emergence until the eruption. Generally, the behavior is similar to that of the 2013 event of §4, with the region emerging and then the poles of the region separating, and then the poles retracting in on themselves, with cancelation occurring at the location of the main neutral line. By the time of the eruption (Fig. 9(f)), the flux has clearly declined markedly from the earlier displayed times.

Figure 10 is analogous to Figure 5, showing in a time-distance map the evolution of the positive and negative fluxes with time. We created the map by integrating along the north-south direction in the box of Fig. 9, and so in this case the vertical axis of Figure 10 represents distance along the x-direction in the panels of Figure 9. This shows that, although the bulk of the flux of the region still remains, some portion of the emerged flux has undergone cancelation by the time of the eruption (orange line).

Figure 11 shows quantitatively the amount of positive-flux reduction over the life of the region, where we have again selected only the positive flux because it is (somewhat) easier to isolate than the negative flux of this region, where we have integrated that positive flux as a function of time over the location of the white box of Figure 9(a). Again we have divided by the cosine of the region's angle with disk center as a function of time. As with the previous event, there again is an overall trend of flux reduction with time. Inspection of AIA 1600 Å, 1700 Å, and 4500 Å images together with the magnetograms shows that a small positive-polarity spot appears near the time of emergence on July 11, and while it fades to a small pore by the end of July 12, HMI magnetograms show that the concentrated

positive flux of the spot continues to disperse over most of the period covered by Figure 11; cancelation of this flux apparently contributes to the steady decrease in positive flux of the region in Figure 11.

Between the start of the decline at about 20 UT on July 11 and the eruption onset time of 15:00 UT on July 16, the flux drops from 8.2×10^{20} Mx to 4.0×10^{20} Mx, so the total reduction is 4.2×10^{20} Mx. Thus, over the 115-hr time period this is a rate of $\sim 3.7 \times 10^{18}$ Mx/hr (and we assume an uncertainty of about the same level as in the first event: 0.2×10^{18} Mx/hr), and the total decrease is about 50% of the peak value.

Again we can estimate the energy built up in the expected flux rope (or sheared field) resulting from the cancelation, again assuming that the canceled flux (4.2×10^{20} Mx) goes into a flux rope. Using magnetograms to estimate the flux rope size, from Figure 9(e) we take its length to be $40''$, and we again use a width of $5''$. Following the procedure in §4.2, here we obtain $B \sim 400$ G. These values result in an estimate for the energy, $VB^2/(8\pi)$, to be 2.4×10^{30} erg, and so similar to that of the 2013 event. With the previous provisos, we again conclude that $\sim 10^{30}$—10^{31} erg of energy could have been accumulated from the cancelation.

From the long-duration 304 Å movie accompanying Figure 7, we see that the filament of the region began to form from about 10:00 UT on July 14, with increased rate of formation from about 12:45 UT on July 15, and full formation by 00:00 UT on July 16. Due to the data dropout over the second-half of July 14, what happens with the magnetic field during that time period is not clear in Figure 10; that figure does however show cancelation at the bipole's main neutral line occurring during the second-half of July 15, consistent with that cancelation leading to the filament's formation. Similarly, cancelation is apparent along that neutral line in the long-duration 304 Å movie with overlaid magnetograms accompanying Figure 7, from about 22:00 UT on July 15 following a data gap.

6. Summary and Discussion

We have followed two different small ARs, from the time that they emerged near the solar east limb, until a time when they were the source for CME-producing eruptions. In both cases: (1) the ARs emerged, (2) their poles moved away from each other until reaching a maximum separation, (3) after that the poles started to retract in on themselves (shown well in Figs. 5 and 10), (4) after some time this retraction led to magnetic flux cancelation along the main neutral line of the emerged bipole, and (5) eventually the continued cancelation led to an eruption along the main neutral line of the retracted bipole. In the 2013 AR of §4, some of the positive flux on the outskirts of the emerging flux region canceled with nearby negative-polarity flux, and the prominent EUV filament of the region formed at that location, which was east of the main (central) neutral line of the AR. In that case, the first eruption was of a (faint in EUV) flux rope that formed along the main neutral line as a result of the cancelation of the retracting region, and that blowout core eruption apparently triggered eruption of the prominent EUV filament a few minutes later, plausibly via the Hudson effect. In the 2010 AR of §5, a filament developed along the main (central) neutral line of the emerged/retracted AR, and it was that filament that erupted to generate the CME.

Figures 3(b) and 7(b) show that the CMEs from these two small AR eruptions had widths of $\sim$60° and 35°. Not all coronal jets produce ejections observable in coronagraphs, but when they do, typically coronal jets produce coronal ejections that are substantially narrower than this, being $\lesssim$10°, and called "white-light jets" or "narrow CMEs" (Wang et al. 1998; Wang & Sheeley 2002; Nisticò 2009; Paraschiv et al. 2010; Yu et al. 2014; Moore, Sterling, & Falconer 2015; Sterling et al. 2016). In some cases, jets can trigger wider CMEs to erupt, when the magnetic field that erupts to drive those jets, i.e. the erupting minifilament (or, presumably an "empty minifilament field" (flux rope) alone, if there is

no cool minifilament material on that field), erupts into the base of a coronal loop and drives that loop out (via its magnetic twist transferred to the loop) to form a CME wider than 10°. Because that larger coronal loop often forms the base of a coronal streamer, we sometimes call these "streamer puff" CMEs (Bemporad et al. 2005; Panesar et al. 2016a). In the two small-AR CMEs studied here, the eruption leading to the CMEs originates along the main neutral line of the ARs, rather than off to the side of the main neutral line of the blown-out loops as is characteristic of streamer puff CMEs. Therefore, the CMEs produced by the two small ARs of this study differ from the narrow CMEs or the streamer puff CMEs that occur with jets. At the same time, from a study by Gopalswamy et al. (2009) of over 10,000 CMEs, the average CME width is 44°, but with a large number wider then 60° (see Fig. 10 of Gopalswamy et al. 2009); hence, the small ARs of this study produced CMEs of relatively moderate width. This is consistent with the idea that the small AR eruptions of this study are on a continuum of solar eruptions occurring on different size scales, with coronal jets being smaller-sized eruptions, and many large-scale eruptions being bigger than those presented here. This also agrees with the trend reported by Moore, Sterling, & Suess (2007) for a direct proportionality between magnetic strength of the area from which the eruption occurs and the final width of the ejected CME.

An initial motivation for this investigation was our previous conclusions that many if not all coronal jets are miniature versions of larger-scale CME-producing eruptions. If this is true, then studying the triggering mechanism of coronal jets (which develop on a short time scale of a couple days or less) could inform us of the triggering mechanism of larger-scale eruptions (which develop on longer timescales, sometimes one or more solar rotations). We found strong evidence that magnetic flux cancelation builds and triggers the CME-producing eruptions for both of our studied small ARs, supporting the suggestion that coronal jets are useful proxies for studying the onset of larger-scale eruptions.

Additionally, we found evidence that filaments in both of our small ARs formed via flux cancelation. This has been found for large-scale filaments previously (see §1). More recent observations show that flux cancelation also builds minifilaments that erupt to drive jets (Panesar et al. 2017). Thus, our results here regarding filaments forming at cancelation sites also supports that there is a continuum of similarly-produced filament-like features on a variety of size scales that erupt.

The two small eruptions of this study do show some differences from the minifilaments that erupt to produce jets; among these is the source of the cancelation that produces the eruptions of this study, compared to the minifilaments in the jet studies. Panesar et al. (2017) found that, for the cases where they could make a determination, the eventually-erupting minifilaments form (a) when tiny grains of flux coalesce to form a minority polarity in a background majority-polarity region; or (b) the minority-polarity pole of a small emerging bipole forms a bipole with a surrounding majority-polarity flux clump, and the minifilament forms along the neutral line of that bipole. In both of the cases presented here, the core erupting feature (a faint flux rope in the 2013 case, and a well-defined filament/flux rope in the 2010 case) both formed when the two poles of the emerged AR retracted in upon themselves, and underwent flux cancelation at the main neutral line of that same previously-emerged bipole. For the AR jets studied by Sterling et al. (2017), the jets occurred in a homologous fashion according to scenario (b). For the AR jets of Sterling et al. (2016) however, at least one of the jets (see §3.5 of Sterling et al. 2016) appears to have occurred along the internal neutral line of a sheared-core emerged bipole, similar to the two events of the present paper.

Because we suspect that the events here are larger-scale versions of coronal jets, and because both the CME-producing eruptions of this paper and many jets result from flux cancelation, we can compare our flux changes for the two events here with those of coronal

jets. We present these comparisons in Table 1 for coronal hole (CH) jets, quiet Sun (QS) jets, AR jets, and the two small CME-producing eruptions of this paper. From this table, it appears that the *rate* of flux cancelation does not seem to be a determinate for the size of the eruption that will occur, since the 2010 small-AR eruption made an eruption apparently more energetic (10^{30}—10^{31} erg) than the AR jets of Sterling et al. (2017) (10^{28}—10^{29} erg), while the rate of flux cancelation in that 2010 small AR (4×10^{18} Mx/hr) was smaller than that of those AR jets (1.5×10^{19} Mx/hr).

Rather, the results suggest instead that the total *percentage* of flux of the entire region that cancels may be more indicative of when an eruption may occur. Although the range of values is large for the jets and the number of AR studied is small, currently the data indicate that by the time ∼50% of the flux of an isolated bipolar region has canceled, that region will either have already erupted or eruption is imminent. This suggests a physical explanation for the possible relationship between flux-cancelation amount and eruption onset: it could be that it is necessary for about 50% of the region's total flux to cancel for enough free energy to be built up in the flux rope (or sheared field), together with the field restraining the eruption (the non-canceled field) to be weak enough, for the eruption to take place. This suggests that, at least for regions that are sufficiently magnetically isolated from their surroundings, monitoring the change in the amount of total flux of a potentially erupting region — up to and including large CME-producing regions — could provide a prognosticator for when eruption will eventually take place. It will however be necessary to investigate additional events before drawing firm conclusions regarding these speculations.

A.C.S. and R.L.M. were supported by funding from the Heliophysics Division of NASA's Science Mission Directorate through the Heliophysics Guest Investigators (HGI) Program, and the *Hinode* project. N.K.P's research was supported by an appointment to the NASA Postdoctoral Program at NASA MSFC, administered by Universities Space

Research Association under contract with NASA.

REFERENCES

Adams, M., Sterling, A. C., Moore, R. L., & Gary, G. A. 2014, ApJ, 783, 11

Bemporad, A., Sterling, A. C., Moore, R. L., & Poletto, G. 2005, ApJ, 635L, 189

Bernasconi, P. N., Rust, D. M., & Hakim, D. 2005, Sol. Phys., 228, 97

Bevington, P. R., & Robinson, D. K. 2003, Data Reduction and Error Analysis (3rd ed.; New York, NY: McGraw-Hill)

Cirtain, J. W., Golub, L., Winebarger, A. R., et al. 2007, Science, 318, 1580

Freeland, S. L., & Handy, B. N. 1998, Sol. Phys., 182, 497

Gopalswamy, N. et al. 2009, Earth, Moon, and Planets, 104 (1-4), 295.

Hong, J., Jiang, Y., Zheng, R., Yang, J., Bi, Y., & Yang, B. 2011, ApJ, 738L, 20

Hong, J., Jiang, Y., Yang, J., Yang, B., Xu, Z., & Xiang, Y. 2016, ApJ, 830, 60

Hong, J., Jiang, Y., Jiayan, Y., Yang, J., Li, H., & Xu, Z., 2017, ApJ, 835, 35

Huang, Z., Madjarska, M. S., Doyle, J. G., & Lamb, D. A. 2012, A&A, 548, A62

Hudson, H. S. 2000, ApJ, 531L, 75

Innes, D. E., & Teriaca, L. 2013, Sol. Phys., 282, 453

Janse, Å. M., & Low, B. C. 2007, A&A, 472, 957

Joshi, N. C., Liu, C., Sun, X., Wang, H., Matara, T., & Moon, Y.-J. 2015, ApJ, 812, 50

Joshi, N. C., Sterling, A. C., Moore, R. L., Magara, T., & Moon, Y.-J. 2017, ApJ, 845, 26

Kumar, P., Karpen, J. T., Antiochos, S. K., Wyper, P. F., DeVore, C. R., & DeForest, C. E. 2018, ApJ, 854, 155

Lemen, J. R., Title, A. M., & Akin, D. J. et al. 2012, Sol. Phys., 275, 17

Li, H., Jiang, Y., Yang, J., Yang, B., Xu, Z., Hong, J., & Bi, Y. 2017, ApJ, 836, 131

Li, H., Yang, J., Jiang, Bi, Y., Qu, Z., & Chen, H. 2018, Ap. and Space Sci., 363, 26

Martin, S. F. 1986, in "Coronal and Prominence Plasmas, ed. A. I. Poland (NASA CP-2442), p. 73

Masson, S., Pariat, E., Aulanier, G., & Schrijver, C. J. 2009, ApJ, 700, 559

Moore, R. L., Sterling, A. C., & Suess, S. T. 2007, ApJ, 668, 1221

Moore, R. L., Sterling, A. C., & Falconer, D. A. 2015, ApJ, 806, 11

Moore, R. L., Sterling, A. C., & Panesar, N. K., ApJ, in press

Mulay, S. M., Tripathi, D., Del Zanna, G., & Mason, H. 2016, A&A, 589, A79

Nisticò, G., Bothmer, V., Patsourakos, S., & Zimbardo, G. 2009, Sol. Phys., 259, 87

Panesar, N. K., Innes, D. E., Tiwari, S. K, & Low, B. C. 2013, A&A, 549, 105

Panesar, N. K., Sterling, A. C., Moore, R. L., & Chakrapani, P. 2016a, ApJ, 832, L7

Panesar, N. K., Sterling, A. C., & Moore, R. L. 2016b, ApJ, 822, 23L

Panesar, N. K., Sterling, A. C., & Moore, & R. L. 2017, ApJ, 844, 131

Panesar, N. K., Sterling, A. C., & Moore, & R. L. 2018, ApJ, 853, 189

Paraschiv, A. R., Lacatus, D. A., Badescu, T., Lupu, M. G., Simon, S., Sandu, S. G., Mierla, M., & Rusu, M. V. 2010, Sol. Phys., 264, 365

Pucci, S., Poletto, G., Sterling, A. C., & Romoli, M. 2013, ApJ, 776, 16

Raouafi, N.-E., Petrie, G. J. D., Norton, A. A., Henney, C. J., & Solanki, S. K. 2008, ApJ, 682, L137

Raouafi, N. E., Patsourakos, S., Pariat, E., et al. 2016, SSRv, 201, 1

Savcheva, A., Cirtain, J. W., DeLuca, E. E., et al. 2007, PASJ, 59S, 771S

Scherrer, P. H., et al. 2012, Sol. Phys., 275,207

Shen, Y., Liu, Y. E., Su, J., & Deng, Y. 2012, ApJ, 745, 164

Shimojo, M., Hashimoto, S., Shibata, K., Hirayama, T., Hudson, H. S., & Acton, L. W. 1996, PASJ, 48, 123

Shimojo, M., & Shibata, K. 2000, ApJ, 542, 1100

Sterling, A. C., Moore, R. L., Falconer, D. A., & Knox, J. M. 2014, ApJ, 788L, 20

Sterling, A. C., Moore, R. L., Falconer, D. A., & Adams, M. 2015, Nature, 523, 437

Sterling, A. C., Moore, R. L., Falconer, D. A., et al. 2016, ApJ, 821, 100

Sterling, A. C., Moore, R. L., Falconer, D. A., Panesar, N. K., & Martinez, F. 2017, ApJ, 844, 28

Sun, X., et al. 2012, ApJ, 748, 77

Török, T., Panasenco, O., Titov, V. S, Mikić, Reeves, K. K., Velli, M., Linker, J. A., & De Toma, G. 2011, ApJ, 739, L63

Wang, Y.-M., Sheeley, N. R., Jr., Socker, D. G., et al. 1998, ApJ, 508, 899

Wang, Y.-M., & Sheeley, N. R., Jr. 2002, ApJ, 575, 542

Young, P. R., & Muglach, K. 2014a, Sol. Phys., 289, 3313

Young, P. R., & Muglach, K. 2014b, PASJ, 66, S12

Yu, H.-S, Jackson, B. V., Buffington, A., Hick, P. P., Shimojo, M., & Sakao, N. 2014, ApJ, 784, 166

van Ballegooijen, A. A. & Martens, P. C. H. 1989, ApJ, 343, 971

Table 1: Magnetic properties for coronal jets and for CME-producing small ARs:

Objects	Study	Cancel Rate (10^{18} Mx/hr)	Canceled amount[(a)] (10^{18} Mx)	Percentage	Energy (erg)
CH Jets	Pucci et al. (2013)	—[(b)]	—[(b)]	—[(b)]	10^{26}—10^{27}
CH Jets	Panesar et al. (2018)	0.6	0.5—2.0	45 ± 16[(c)]	—[(b)]
QS Jets	Panesar et al. (2016b)	1.5[(d)]	0.9—4.0	37 ± 13[(e)]	—[(b)]
QS & AR Jets[(f)]	Shimojo & Shibata (2000)	—[(b)]	—[(b)]	—[(b)]	10^{27}—10^{29}
AR Jets	Sterling et al. (2017)	15	5	—	10^{28}—10^{29}
2013 Oct 20	This paper, §4	13	390	29 ± 3[(g)]	$\sim 10^{30}$—10^{31}
2010 Jul 16	This paper, §5	4	420	51 ± 3[(g)]	$\sim 10^{30}$—10^{31}

(a) Total average flux canceled from start of flux decline, or from time of previous events in the case of homologous jets.

(b) This quantity difficult to measure reliably, or otherwise not provided in stated study.

(c) Determined using values in Table 1 of Panesar et al. (2018); see text §2.

(d) Data for this value are from Panesar et al. (2016b), but the calculation is described in §4.1 of Panesar et al. (2018).

(e) Determined using values in Table 1 of Panesar et al. (2016b); see text §2.

(f) Although this study examined jets in all regions, it used *Yohkoh*/SXT data, which were biased toward AR and QS jets over the comparatively-softer-X-ray CH jets.

(g) Uncertainty determined assuming assuming flux values accurate to 2×10^{19} Mx.

Fig. 1.— Schematic showing jet generation via a "minifilament eruption model," as proposed in Sterling et al. (2015) (with an adjustment due to Moore et al. 2018; see text). (a) Cross-sectional view of a 3D positive-polarity anemone-type field inside of a majority negative-polarity ambient background field (which is either open or far-reaching field). One side of the anemone is highly sheared and contains a minifilament (blue circle). (b) Here the minifilament is erupting and undergoing reconnection in two locations: *internal* ("tether-cutting" type) reconnection (larger red X), with the solid red lines showing the resulting reconnected fields; the thick red semicircle represents the "jet-base bright point" (JBP). *External* (a.k.a. "interchange" or "breakout" reconnection) occurs at the site of the smaller red X, with the dashed lines indicating its two reconnection products. (c) If the external reconnection proceeds far enough, then the minifilament material can leak out onto the open/far-reaching field. Shaded areas represent heated jet material visible in X-rays and some *SDO*/AIA EUV channels. See captions of e.g. Sterling et al. (2015) or Moore et al. (2018) for a more detailed description. Labels M1, M2, and M3 are referred to in the text; they respectively point out negative, positive, and negative photospheric polarity locations.

Fig. 2.— AIA 304 Å (a–c; g–i), and 131 Å (d–f) images of a small-AR CME-producing eruption, from 2013 October. Contours in (d) are from an *SDO*/HMI magnetogram from 08:30 UT on October 20, and contours in (h) are from 16:45 UT on October 18, with red and yellow contours respectively representing positive and negative field. Arrows in (a—c) point out a faint flux rope erupting away from the core of the region, where the main neutral line (d) is located. Overall, the basic eruption geometry is analogous to that of the coronal jet in Fig. 1, where the flare brightening along the neutral line in (d) corresponds to the JBP in Figs. 1(b) and 1(c), and where the arrows in (e) point to "external brightenings," corresponding to the footpoints of reconnected loop fields corresponding to the location marked M1 in Fig. 1(a). Arrows in (h) point to a filament that forms along a neutral line

away from the main central neutral line; this filament is erupting in (f) and (i). Animations of this figure are available. There are separate 304 Å animations for (a–c) and for (d–f), with the former being of shorter duration, higher cadence, closer-in field of view, and different color and intensity scalings than the latter, with parameters of the former tuned to facilitate viewing of the faint flux rope. In these and all other solar images in this paper, north is up and west is to the right. For the event shown here, and in all other figures for this 2013 small-AR event, the images were differentially rotated to the common time of 2013 October 20, 09:00 UT.

Fig. 3.— *SOHO*/LASCO/C2 running difference image of the CME accompanying the eruption of Fig. 2. White lines in (b) subtend an angle of $\approx 60°$. An animation of this figure is available.

Fig. 4.— Magnetic flux changes from HMI of the region of Fig. 2, with white/black representing positive/negative fluxes, respectively. The box in (a) shows the region used to produce the flux plot in Fig 5. Fluxes saturate at ±300 G. Arrows in (b) show examples of mid-strength flux elements that cancel to form the filament that erupts in Fig. 2(f). An animation of this figure is available.

Fig. 5.— Time-distance map for the event of Fig. 2 for the flux summed in the horizontal (E-W) direction (i.e., in pixel rows) over the box of Fig. 4(a). Flux emerges near the start; the two poles spread apart, reaching a maximum separation near 0 UT on 19 Oct; and then the two poles converge back on themselves, with cancelation occurring at the central neutral line of the bipole from approximately the start of October 20. A CME-producing eruption occurred near 08:00 UT on October 20. Blue dashed lines indicate 00:00 UT for each day, and the solid orange line shows the time of the eruption.

Fig. 6.— Variation with time of positive flux for the event of Fig. 2, where the flux is the

integrated positive-polarity flux over the box in Fig. 4(a). Values are calculated assuming a field component vertical to the surface, where we have approximately corrected for foreshortening by dividing by the cosine of the angle between the region and observed disk center (see text). The green line is a least-square fit over the period of the decay until the eruption (from 19 October 05:30 UT until 20 October 11:45 UT), and the orange line marks the onset time of the flare/CME-producing eruption.

Fig. 7.— AIA Å and 304 Å images of a second small CME-producing eruption of this study, this one from July 2010. Contours in (a) are from an HMI magnetogram from 15:15 UT on July 16, and contours in (e) are from 09:45 UT on the same day, with red and blue contours respectively representing positive and negative field. In this case the filament is erupting nearly directly out of the figure; arrows in (b) and in (e) point to the filament. Animations of this figure are available. Jumps in time during the last half of July 14 in the animations are due to *SDO* spacecraft pointing changes. For the event shown here, and in all other figures for this 2010 small-AR event, the images were differentially rotated to the common time of 2010 July 16, 15:30 UT.

Fig. 8.— *STEREO*/COR1 running difference image of the CME accompanying the eruption of Fig. 7. White lines in (b) subtend an angle of $\approx 35°$. An animation of this figure is available.

Fig. 9.— As in Fig. 4, but for the event of Fig. 7. The box in (a) shows the region used to produce the flux plot in Fig. 9. Fluxes saturate at ±300 G. An animation of this figure is available. Jumps in time during the last half of July 14 in the animation are due to *SDO* spacecraft pointing changes.

Fig. 10.— Time-distance map, as in Fig. 5 but for the event of Fig. 7, where the flux is summed along pixel columns in the vertical (N-S) direction of the box of Fig. 7(a). The

vertical strip during the last half of July 14 is an artifact resulting from *SDO* spacecraft operations during that period, and so that portion of the map should be ignored. A CME-producing eruption occurred near 15:00 UT on July 16; the solid orange line shows the eruption time.

Fig. 11.— Variation with time of positive flux for the event of Fig. 7, where the positive flux is integrated over the box in Fig. 7(a). Values are calculated assuming a field component vertical to the surface, where we have approximately corrected for foreshortening by dividing by the cosine of the angle between the region and observed disk center (see text). The green line is a least-square fit over the period of the decay until the eruption (from 19 October 05:30 UT until 20 October 11:45 UT), and the orange line marks the onset time of the flare/CME-producing eruption.

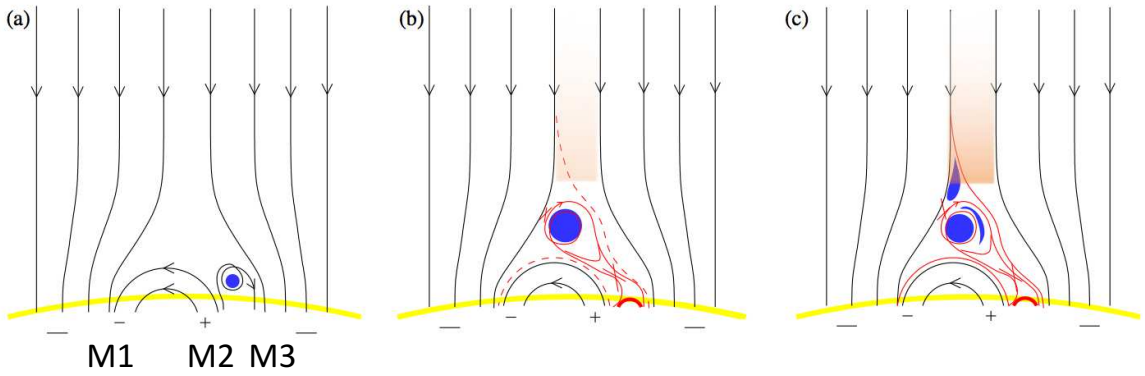

Figure 1

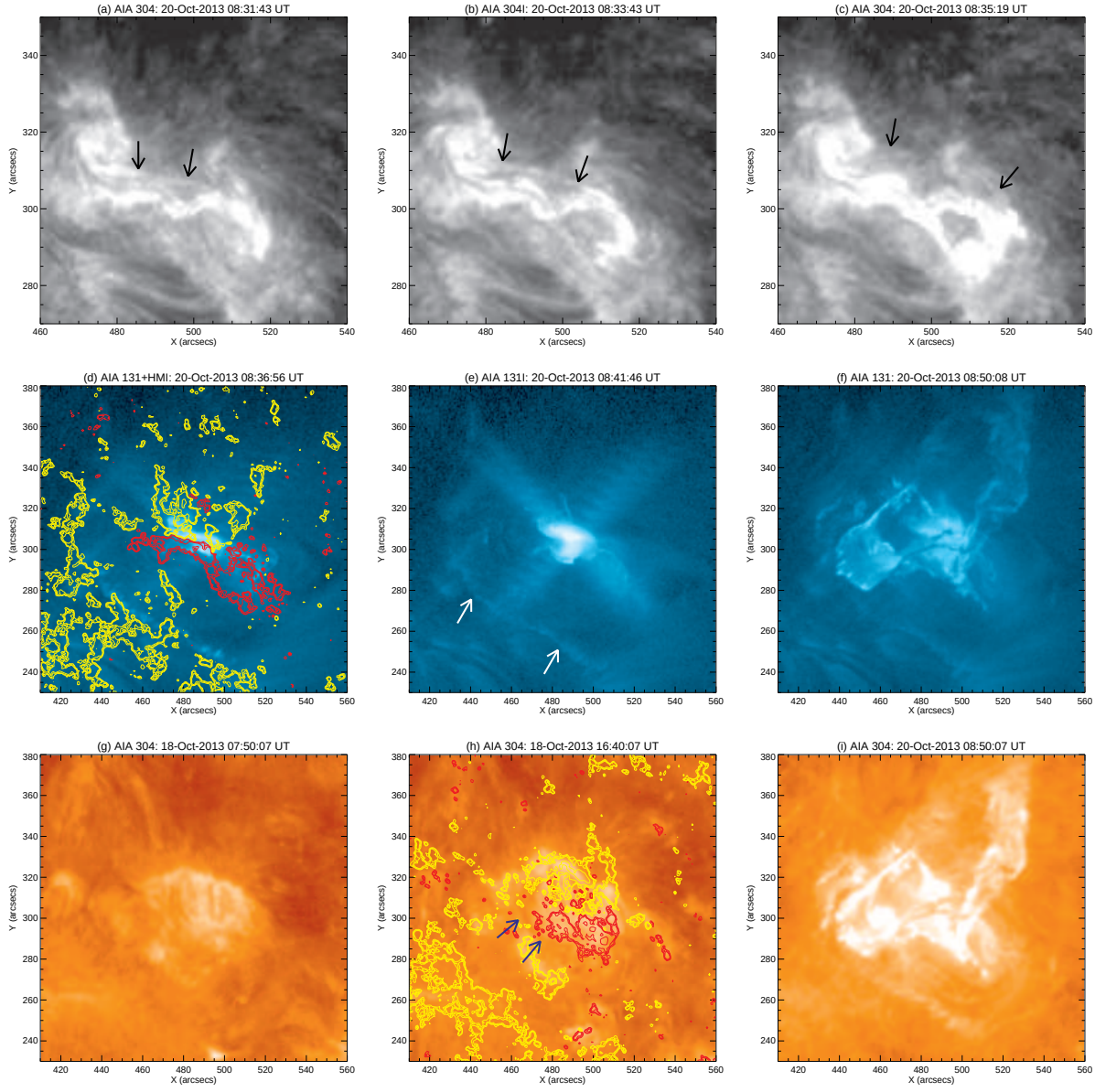
(a) AIA 304: 20-Oct-2013 08:31:43 UT
(b) AIA 304I: 20-Oct-2013 08:33:43 UT
(c) AIA 304: 20-Oct-2013 08:35:19 UT
(d) AIA 131+HMI: 20-Oct-2013 08:36:56 UT
(e) AIA 131I: 20-Oct-2013 08:41:46 UT
(f) AIA 131: 20-Oct-2013 08:50:08 UT
(g) AIA 304: 18-Oct-2013 07:50:07 UT
(h) AIA 304: 18-Oct-2013 16:40:07 UT
(i) AIA 304: 20-Oct-2013 08:50:07 UT
X (arcsecs)
Y (arcsecs)

Figure 2

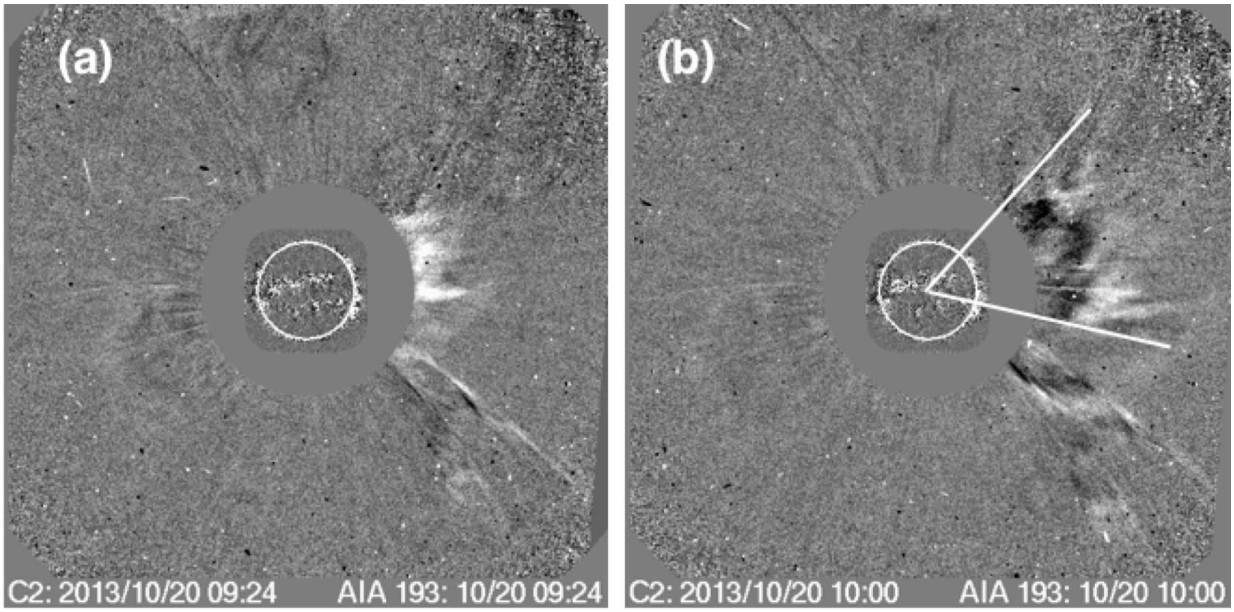
(a)
C2: 2013/10/20 09:24
AIA 193: 10/20 09:24
(b)
C2: 2013/10/20 10:00
AIA 193: 10/20 10:00

Figure 3

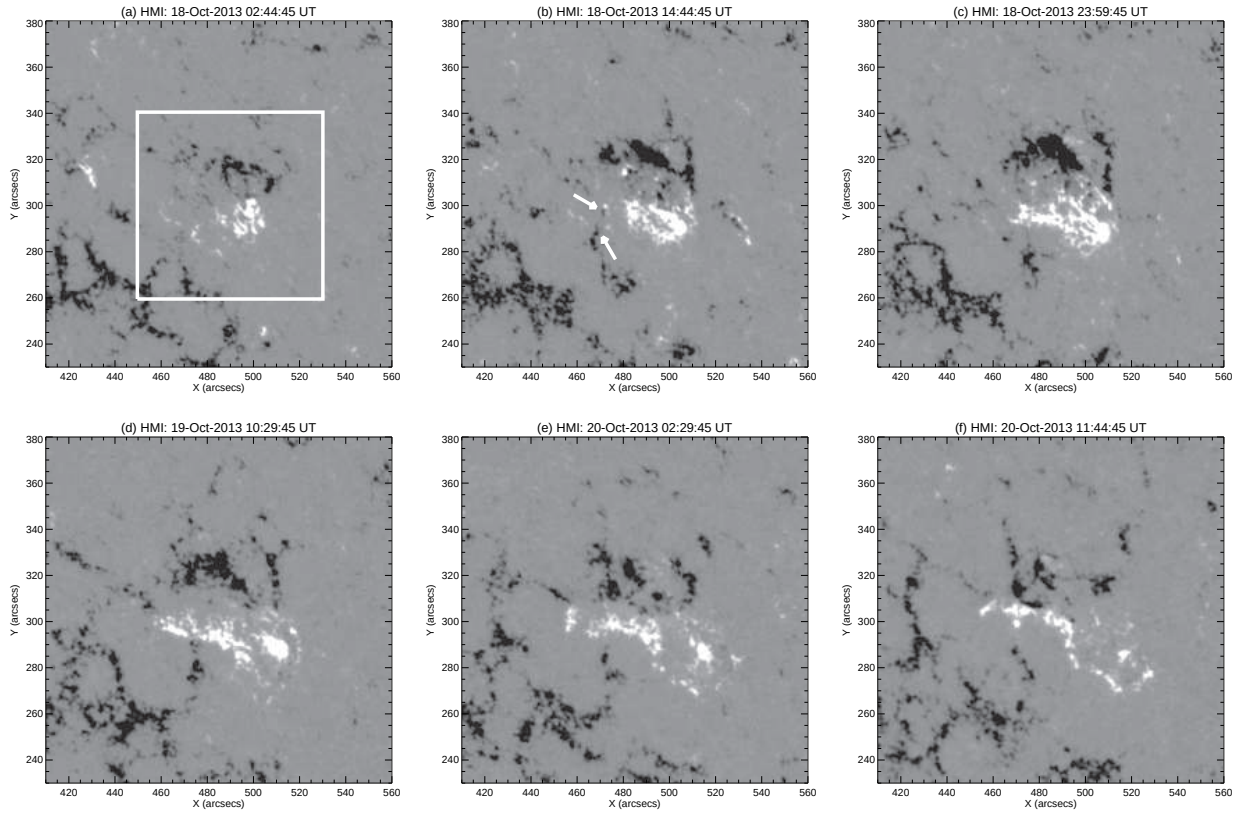
(a) HMI: 18-Oct-2013 02:44:45 UT
(b) HMI: 18-Oct-2013 14:44:45 UT
(c) HMI: 18-Oct-2013 23:59:45 UT
(d) HMI: 19-Oct-2013 10:29:45 UT
(e) HMI: 20-Oct-2013 02:29:45 UT
(f) HMI: 20-Oct-2013 11:44:45 UT
Y (arcsecs)
X (arcsecs)
240
260
280
300
320
340
360
380
420
440
460
480
500
520
540
560

Figure 4

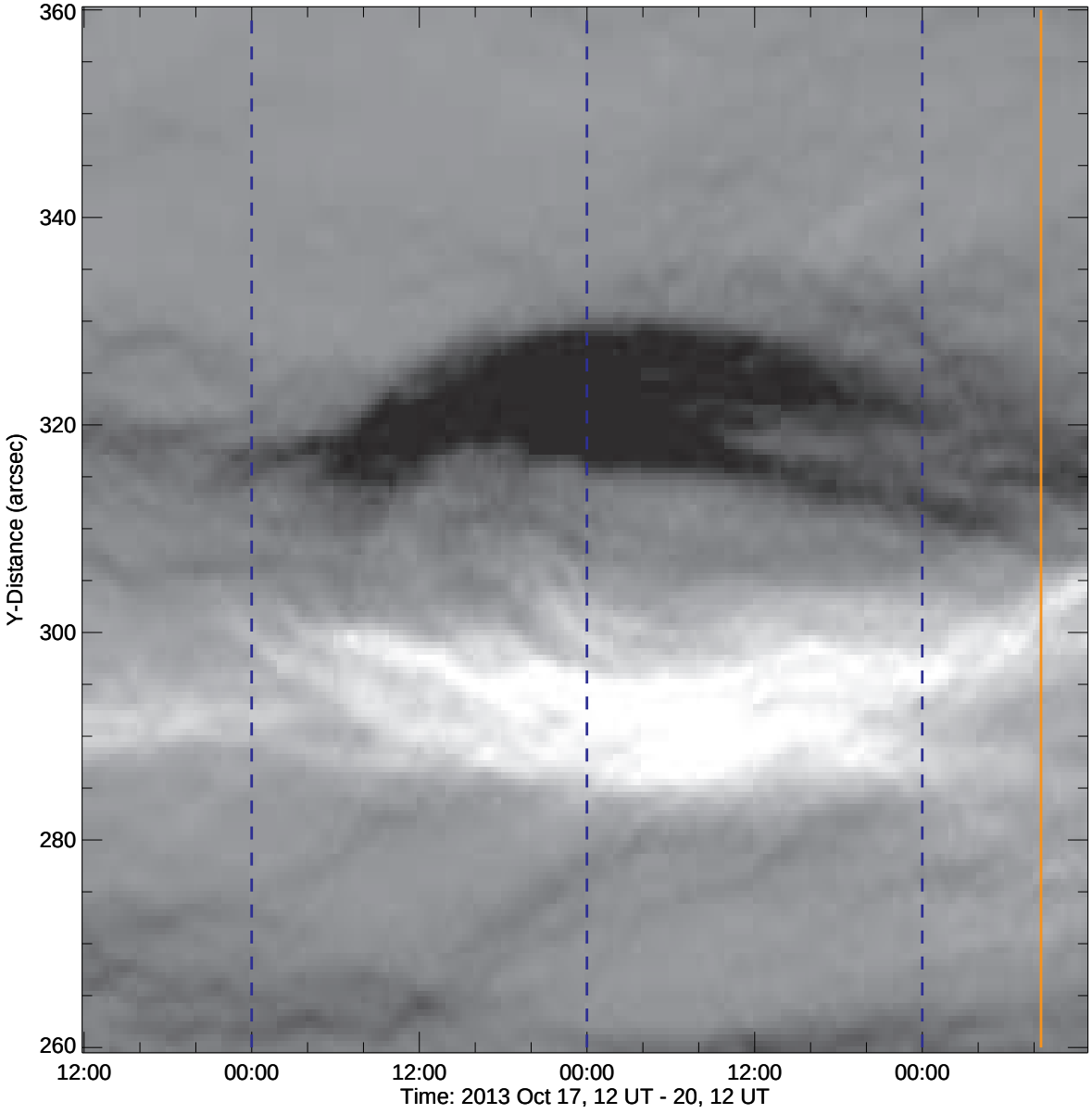
360
340
320
300
280
260
Y-Distance (arcsec)
12:00
00:00
12:00
00:00
12:00
00:00
Time: 2013 Oct 17, 12 UT - 20, 12 UT

Figure 5

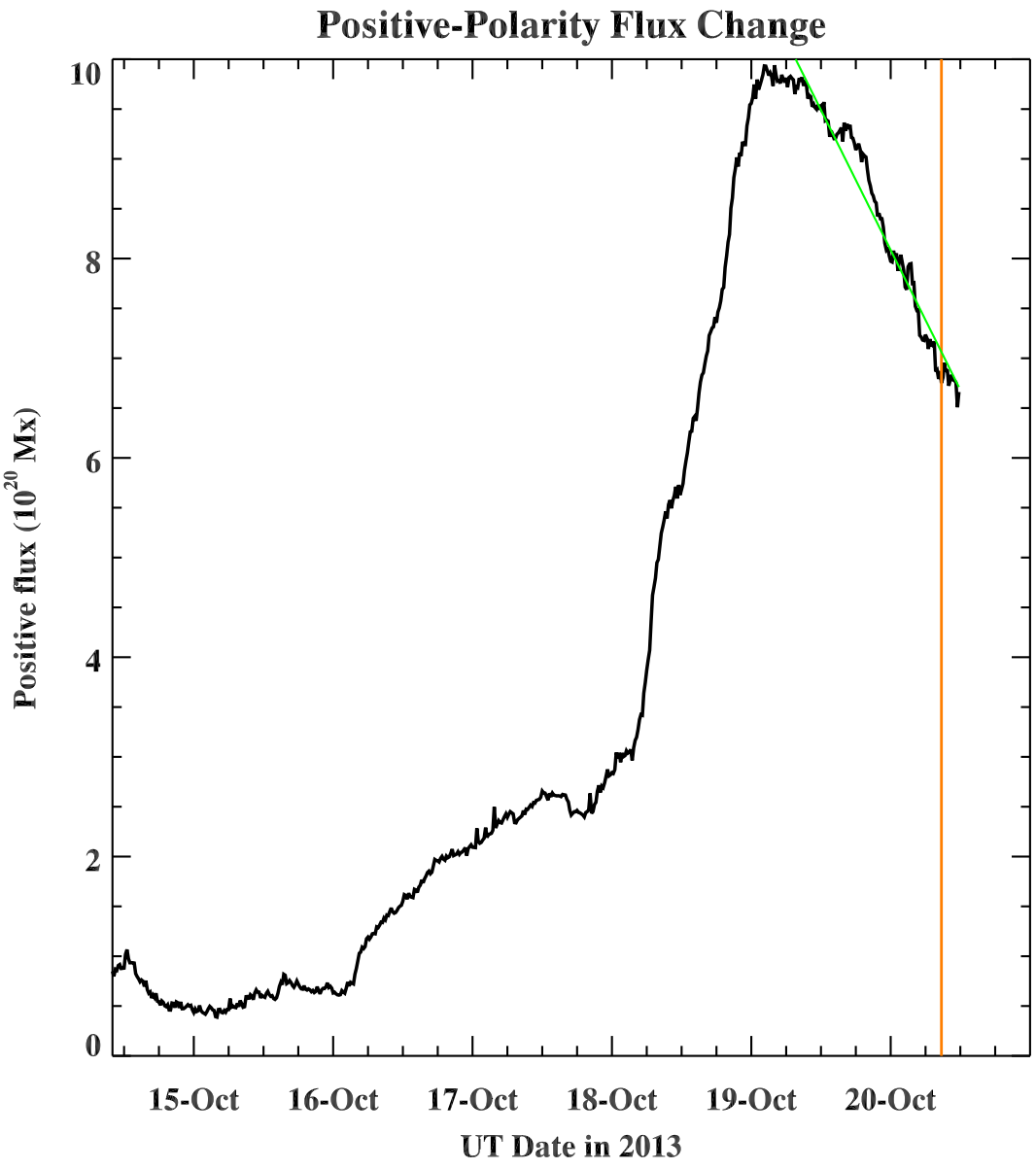
Positive-Polarity Flux Change
Positive flux (10^{20} Mx)
0
2
4
6
8
10
15-Oct
16-Oct
17-Oct
18-Oct
19-Oct
20-Oct
UT Date in 2013

Figure 6

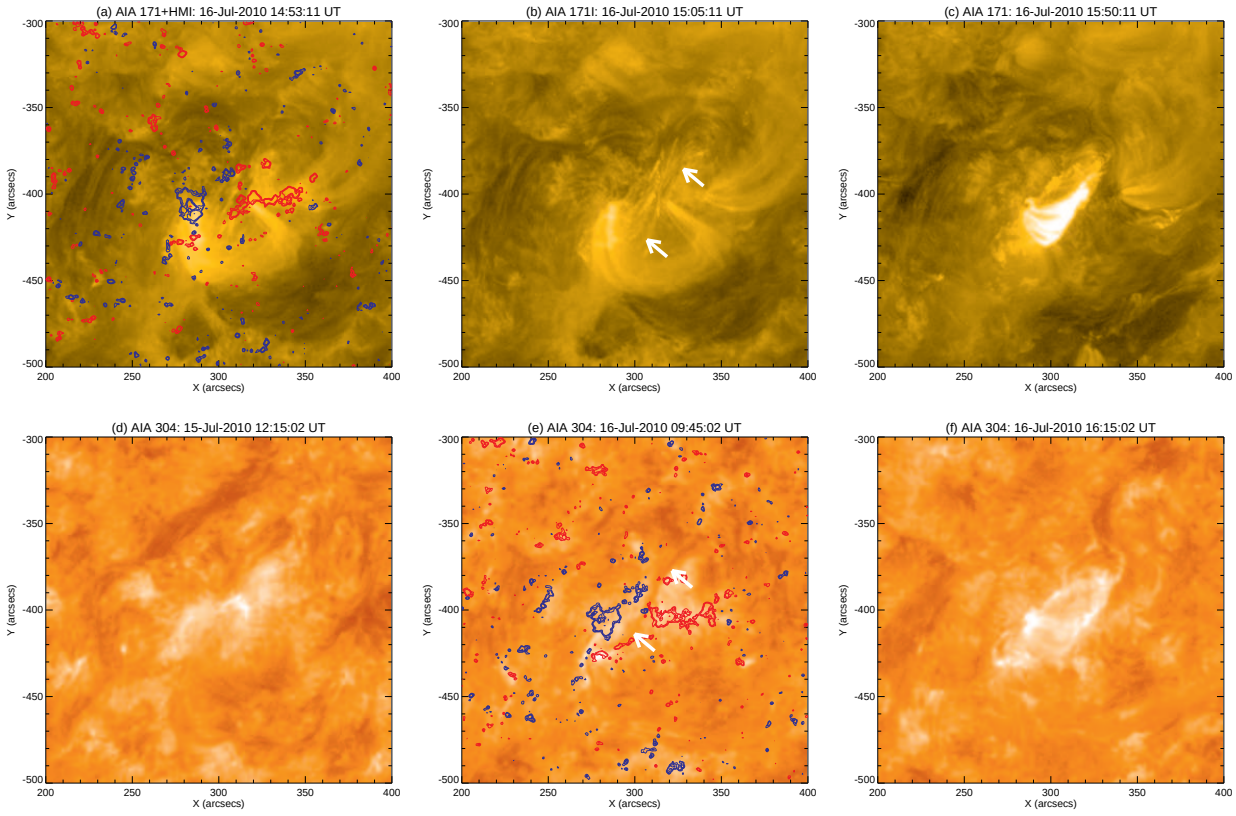
(a) AIA 171+HMI: 16-Jul-2010 14:53:11 UT
(b) AIA 171I: 16-Jul-2010 15:05:11 UT
(c) AIA 171: 16-Jul-2010 15:50:11 UT
(d) AIA 304: 15-Jul-2010 12:15:02 UT
(e) AIA 304: 16-Jul-2010 09:45:02 UT
(f) AIA 304: 16-Jul-2010 16:15:02 UT
Y (arcsecs)
X (arcsecs)
-300
-350
-400
-450
-500
200
250
300
350
400

Figure 7

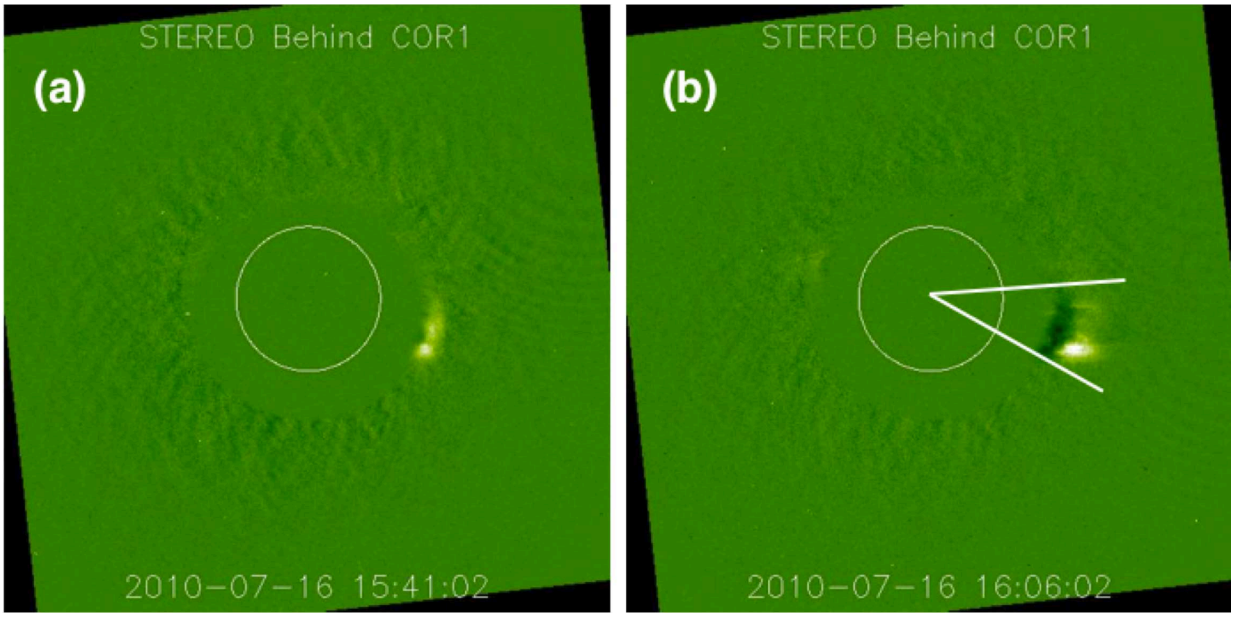
STEREO Behind COR1
(a)
2010-07-16 15:41:02
STEREO Behind COR1
(b)
2010-07-16 16:06:02

Figure 8

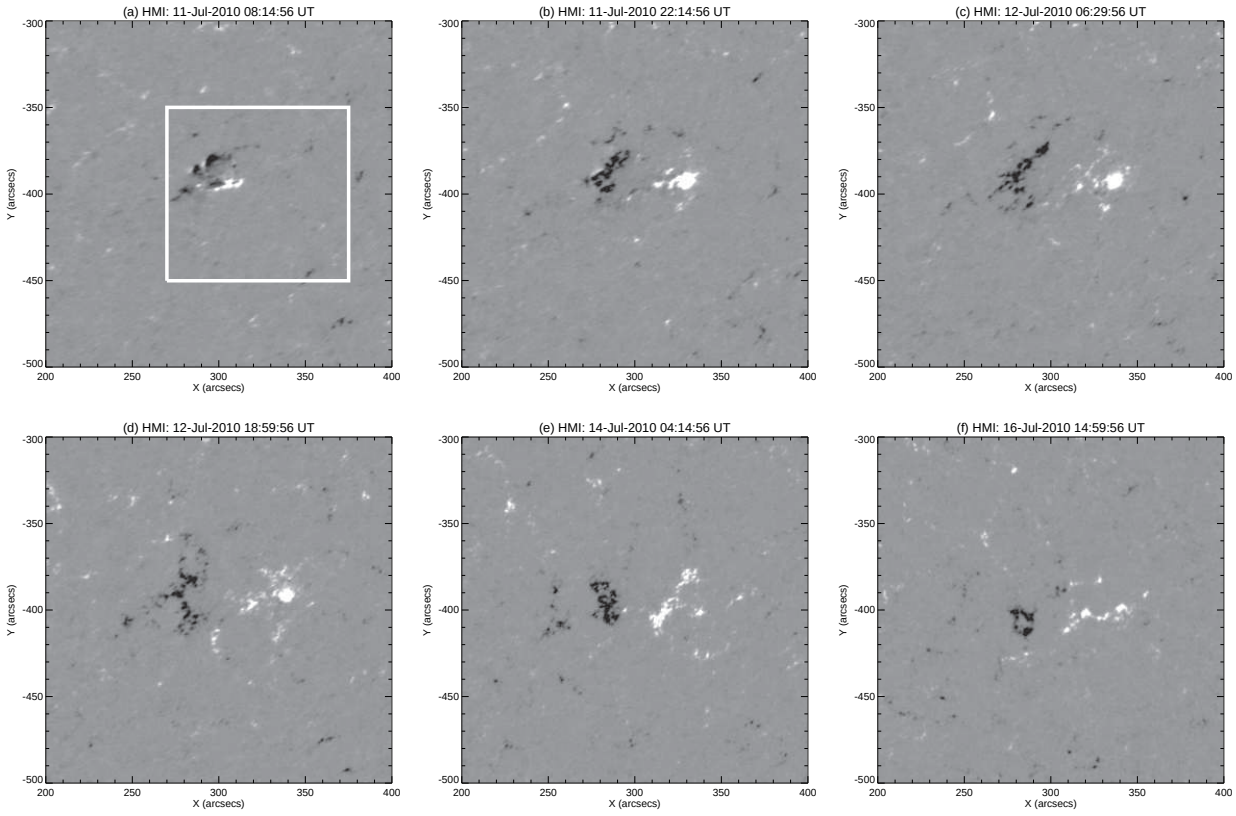
(a) HMI: 11-Jul-2010 08:14:56 UT
(b) HMI: 11-Jul-2010 22:14:56 UT
(c) HMI: 12-Jul-2010 06:29:56 UT
(d) HMI: 12-Jul-2010 18:59:56 UT
(e) HMI: 14-Jul-2010 04:14:56 UT
(f) HMI: 16-Jul-2010 14:59:56 UT
Y (arcsecs)
X (arcsecs)
-300
-350
-400
-450
-500
200
250
300
350
400

Figure 9

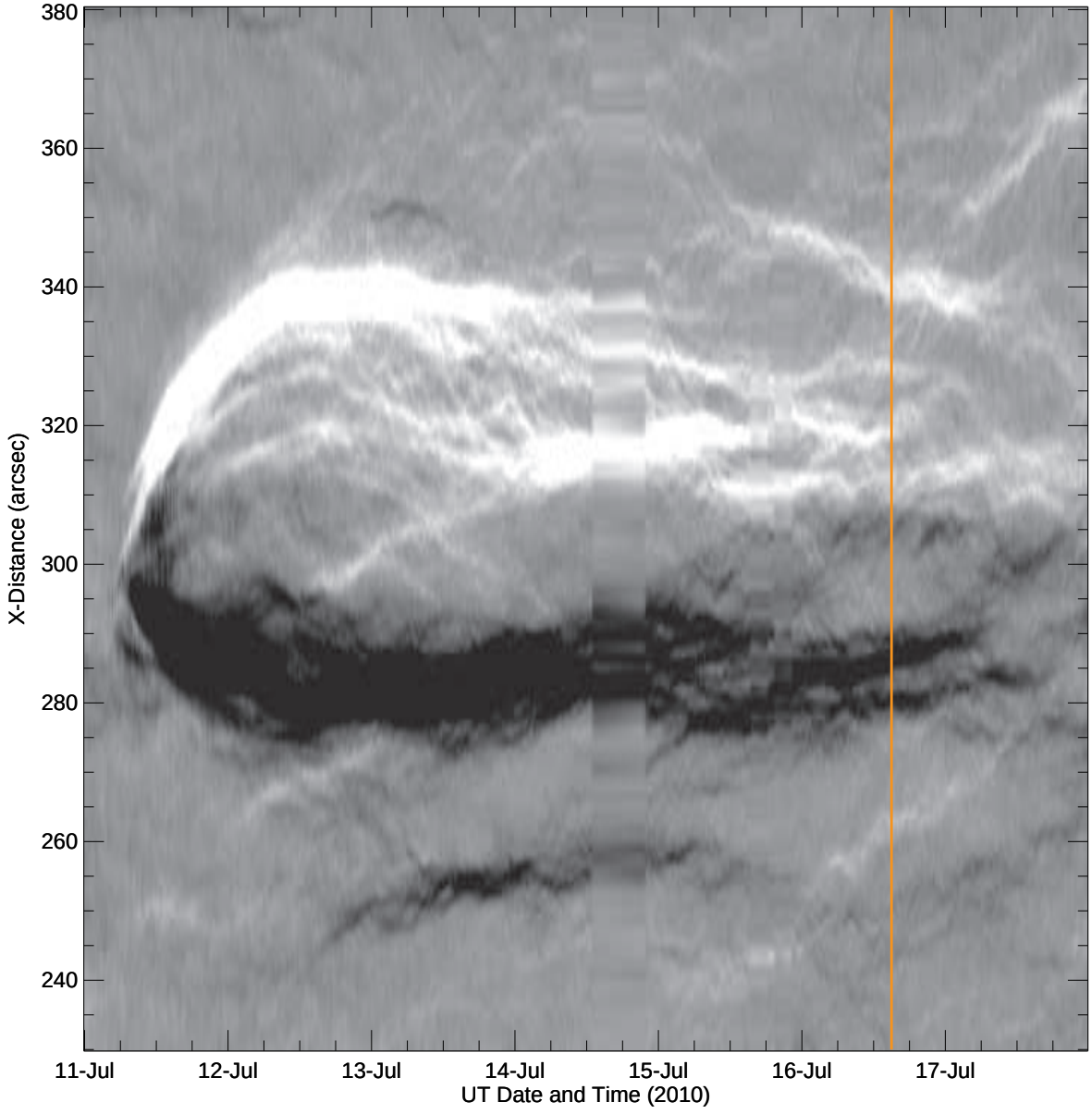
380
360
340
320
300
280
260
240
X-Distance (arcsec)
11-Jul
12-Jul
13-Jul
14-Jul
15-Jul
16-Jul
17-Jul
UT Date and Time (2010)

Figure 10

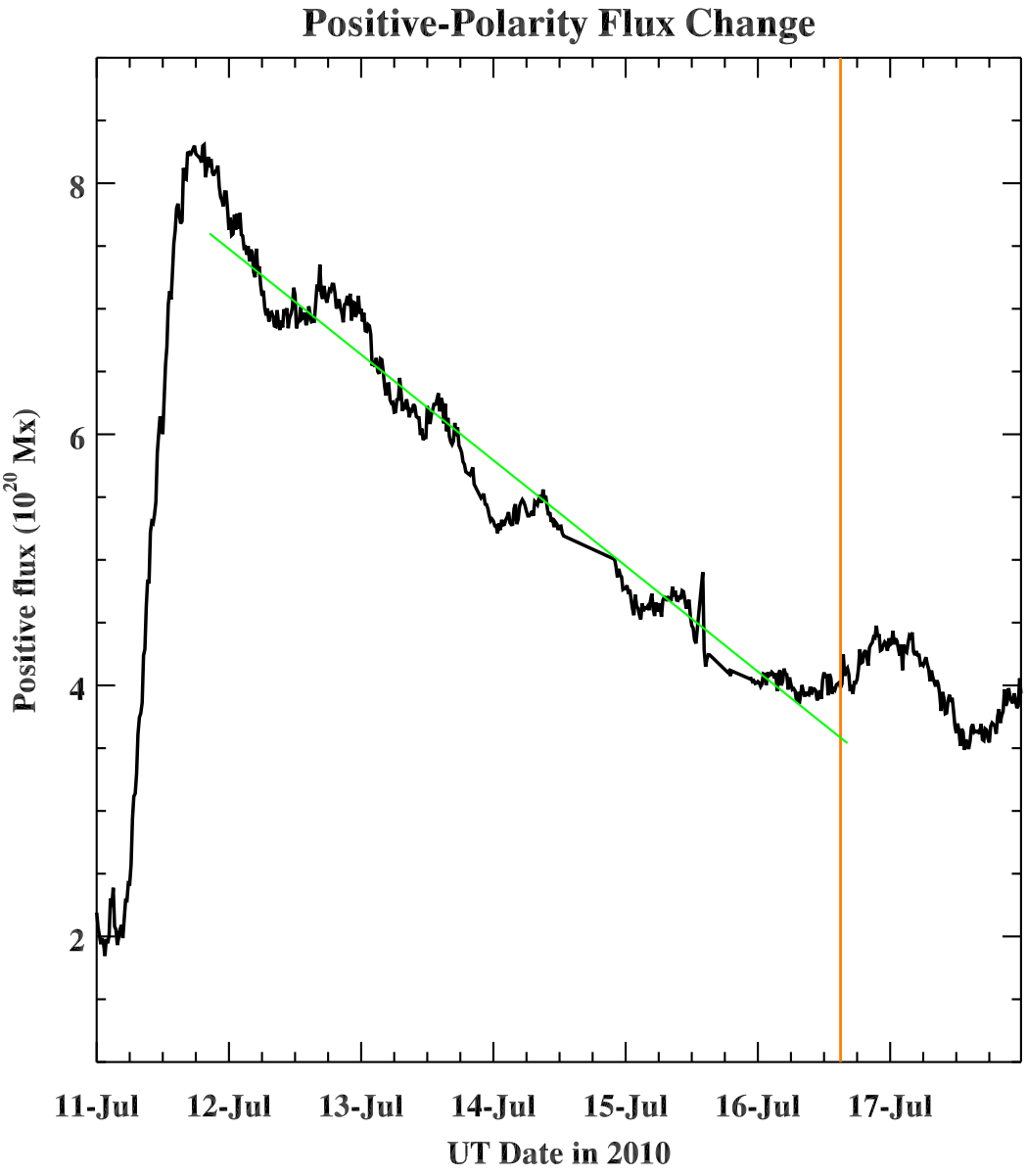
Positive-Polarity Flux Change
Positive flux (10^{20} Mx)
8
6
4
2
11-Jul
12-Jul
13-Jul
14-Jul
15-Jul
16-Jul
17-Jul
UT Date in 2010

Figure 11